

Revealing and Controlling the Core of Screw Dislocations in BCC Metals

Zhaoxuan Wu (✉ zhaoxuwu@cityu.edu.hk)

City University of Hong Kong

Rui Wang

City University of Hong Kong

Lingyu Zhu

City University of Hong Kong

Subrahmanyam Pattamatta

City University of Hong Kong

David Srolovitz

The University of Hong Kong

Physical Sciences - Article

Keywords: Body-centred-cubic transition metals, metal structure, screw dislocation

Posted Date: September 28th, 2021

DOI: <https://doi.org/10.21203/rs.3.rs-879826/v1>

License:  This work is licensed under a Creative Commons Attribution 4.0 International License.

[Read Full License](#)

Revealing and Controlling the Core of Screw Dislocations in BCC Metals

Rui Wang,¹ Lingyu Zhu,¹ Subrahmanyam Pattamatta,¹ D. J. Srolovitz,² and Zhaoxuan Wu^{1,*}

¹*Department of Materials Science and Engineering, City University of Hong Kong, Hong Kong, China*

²*Department of Mechanical Engineering, The University of Hong Kong, Hong Kong, China*

Body-centred-cubic (BCC) transition metals (TMs) tend to be brittle at low temperatures, posing significant challenges in their processing and major concerns for damage tolerance in critical load-carrying applications. The brittleness is largely dictated by the screw dislocation core structure;¹⁻⁵ the nature and control of which has remained a puzzle for nearly a century.^{2,6} Here, we introduce a universal model and a physics-based material index χ that guides the manipulation of dislocation core structure in all pure BCC metals and alloys. We show that the core structure, commonly classified as degenerate (D) or non-degenerate (ND), is governed by the energy difference between BCC and face-centred cubic (FCC) structures and χ robustly captures this key quantity. For BCC TMs alloys, the core structure transition from ND to D occurs when χ drops below a threshold, as seen in atomistic simulations based on nearly all extant interatomic potentials and density functional theory (DFT) calculations of W-Re/Ta alloys.^{7,8} In binary W-TMs alloys, DFT calculations show that χ is related to the valence electron concentration at low to moderate solute concentrations, and can be controlled via alloying. χ can be quantitatively and efficiently predicted via rapid, low-cost DFT calculations for any BCC metal alloys, providing a robust, easily applied tool for the design of ductile and tough BCC alloys.

BCC TMs play pivotal roles in a wide-range of structural and functional applications, including current and future transportation, electronic, chemical and energy generation technologies. They are often employed to withstand extreme mechanical, thermal, chemical and radiative loadings. Their mechanical behaviour, such as yielding, hardening and fracture, are thus critical and have been under intensive research for a century.^{2,6} Extensive experiments show that BCC TMs experience an often-drastic decrease in ductility, i.e., ductile-to-brittle transition (DBT), with decreasing temperature.^{4,9} This temperature-dependent behaviour is mostly controlled by the core structure of the line defects, predominantly $1/2\langle 111 \rangle$ screw dislocations,^{1,10} that carry plastic deformation. For example, screw dislocations in pure W adopt a ND-core structure and preferentially glide on $\{110\}$ planes. This core exhibits gigapascal-scale lattice friction,³ making stress-relieving dislocation plasticity difficult and often leading to brittle fracture.¹ However, W can be drastically ductilized by alloying with Re, which changes the ND-core to the D-core and activates $\{112\}$ slips.^{7,8,11} Controlling core structures and activating additional slip systems are central to enhancing the mechanical response of BCC TMs. However, the physical origin governing the competition between the D- and ND-core structures has remained a mystery despite an intensive search over many decades.^{2,12-15}

DFT-based calculations show that all pure BCC TMs adopt the ND-core structure,^{5,16,17} while those based upon empirical/semi-empirical interatomic potentials exhibit both D- and ND-cores. Different criteria were developed to identify the core-controlling properties. Duesbery and Vitek¹⁸ proposed that the core structure is governed by the generalized stacking fault energy line (γ -line) along $\langle 111 \rangle$ directions on $\{110\}$ planes, i.e., the ND-core is favoured over the D-core if $2\gamma_{b/6} < \gamma_{b/3}$ ($\mathbf{b} = \langle 111 \rangle/2$ is the Burgers vector). However, counter examples defying this criterion are common.^{7,19} The choice of the core structure has also been attributed to the nature of interatomic bonding; strong directional bonding from d-band electrons is required to produce ND-cores, as demonstrated with bond-order potentials (BOP).²⁰ However, Chiesa et al.²¹ showed that directional bonding is not necessary for ND-cores; non-directional interatomic potentials can reproduce ND-cores under certain conditions if they exhibit a double-humped inter-string interaction energy (see Methods). Nevertheless, many potentials (e.g., machine learning-based Gaussian Approximation Potentials, GAP²²) reproduce the ND-core

with a single-hump inter-string interaction energy,^{23,24} demonstrating that the double-hump criterion is not general. The ratio of shear moduli in different directions on the $\{110\}$ plane was proposed as differentiating core structures.² However, no clear trend has been observed across extant simulations. While these suggestions yield tantalising hints about dislocation core structure and behaviour across the BCC TM family, the fundamental question of what controls the core structure remains an important mystery. The *a priori* prediction of dislocation core structure in BCC TMs is key to understanding existing BCC systems and designing new BCC TMs alloys.

Here, we provide a universal model to predict the core structure of all BCC metals and alloys. We show that D-/ND-core structures can be understood from the γ -line along $\langle 110 \rangle$ on $\{110\}$ planes. This insight is related to the energy difference ΔE between FCC and BCC structures and has its origin in crystal geometry.²⁵ We define a new material index for BCC TM alloys $\chi = \Delta E^A / \Delta E^P$, where superscripts A/P represent alloyed/pure BCC TMs. The ND-/D-core structures and slip behaviour can be manipulated by tuning χ through alloying and predicted via rapid DFT calculations. This approach is general and universally applicable to *all* BCC metals and alloys. It also provides a new engineering paradigm for the design of ductile and tough BCC TMs alloys with low DBT temperatures.

A dislocation is characterised by its Burgers vector \mathbf{b} and line direction ξ .²⁶ On a continuum level, \mathbf{b} is defined as $\oint_C (\partial \mathbf{u} / \partial l) dl$, where \mathbf{u} is the displacement vector and the integral dl is along an arbitrary closed path C enclosing the dislocation core. On a discrete level, the contour integral is replaced by a summation along discrete segments k , i.e.,

$$\mathbf{b} = \sum_{k=1}^N (\mathbf{u}_{ij}^{(k)} - \mathbf{U}_{ij}^{(k)}) = \sum_{k=1}^N \mathbf{d}_k, \quad (1)$$

where \mathbf{u}_{ij} and \mathbf{U}_{ij} are displacement vectors between atom i and j before and after the introduction of the dislocation and \mathbf{d}_k is the differential displacement (DD) between atom i and j . Each \mathbf{d}_k contributes a fraction of the total Burgers vector \mathbf{b} .²⁶

In the BCC structure, the screw dislocation Burgers vector \mathbf{b} can be split into three \mathbf{d}_k enclosing the core. Figure 1 shows the core structures and γ -surfaces of BCC Li, Ta and W calculated using DFT (see Methods). Li exhibits a D-core while Ta and W show ND-cores. The core structures are dictated by core energies. The core energy E_c arises primarily from the shear displacements \mathbf{d}_1 , \mathbf{d}_2 , \mathbf{d}_3 in the $\langle 111 \rangle$ direction between neighbouring atoms enclosing the core centre

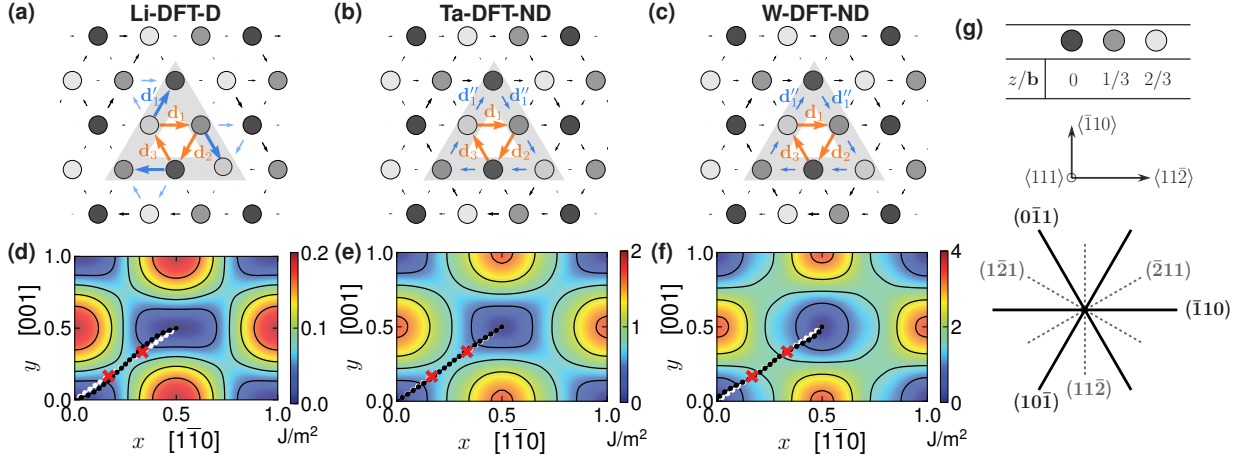


Fig. 1 | Dislocation core structures and γ -surfaces of BCC Li, Ta and W. (a) The D-core of Li. (b-c) The ND-core of Ta and W. (d-f) γ -surface on $\{110\}$ planes of Li, Ta and W. (g) Traces of atom planes in the BCC $\langle 111 \rangle$ -zone. In (a-c), atoms are colored based on their position (see g) in the $\langle 111 \rangle$ (viewing) direction. The core is enclosed inside the gray triangle. Arrows are the DD in the Burgers vector direction. The D-core has three DD vectors $\mathbf{d}'_k \approx \mathbf{b}/3$ (blue arrows) with a $\langle 111 \rangle$ threefold screw axis symmetry. The ND-core has six DD vectors $\mathbf{d}'_k \approx \mathbf{b}/6$ (blue arrows) and possesses both a $\langle 111 \rangle$ threefold screw axis symmetry and a $\langle 110 \rangle$ diad axis symmetry. In (d-f), the black lines are MEP between two perfect lattice positions along the Burgers vector (white lines). The MEP deviates gently from the Burgers vector direction. The red crosses mark respective positions at $\mathbf{b}/3$.

(orange arrows in Fig. 1a-c). This energy cannot be computed based on elasticity, but can be described through the $\langle 111 \rangle / \{110\}$ γ -line (Fig. 1d-f). Typical γ -lines vary smoothly around $\mathbf{b}/3$ (Extended Data Fig. 2), suggesting equal splitting of shear displacements among the three equivalent $\{110\}$ planes.¹⁸ Since the dislocation elastic energy E_e scales as \mathbf{b}^2 , splitting the Burgers vector into three equal fractional Burgers vectors ($\mathbf{b}/3$) is more favourable than other splittings. Thus, it is natural to expect that splitting the shear displacement equally on three equivalent $\{110\}$ planes will lower the total dislocation energy $E_t = E_c + E_e$.

For Li, Ta and W, the current calculations give $\mathbf{d}_1 \cong \mathbf{d}_2 \cong \mathbf{d}_3 \cong \mathbf{b}/3$, as seen in Fig. 1 (Extended Data Fig. 7). This agrees with nearly all previous core structures calculated in BCC TMs, irrespective of the description of atomic interactions⁵ (DFT or interatomic potentials). Therefore, splitting the Burgers vector near the dislocation centre follows equal splitting $\mathbf{d}_k \approx \mathbf{b}/3$ on three equivalent $\{110\}$ planes (for D-/ND-cores); i.e., all core centres appear identical. This core-splitting implies that the core centre (screw components, orange arrows in Fig. 1a-c) fulfils the $\langle 110 \rangle$ -dyad symmetry of the BCC lattice and is thus non-degenerate. Nevertheless, examination of the γ -surface shows that the minimum energy path (MEP, black line in Fig. 1d-f) between two ground states deviates from a $\langle 111 \rangle$ path (white line). This suggests that core energy can be further reduced by core splitting following the MEP and \mathbf{d}_k contains edge components in general.

The principle differences between the D-/ND-cores lie in the details of the \mathbf{d}_k outside the core centre. Applying the topological requirement of Eq. 1, each \mathbf{d}_k is compensated by two more DD vectors in the triangular loop formed by one orange and two blue arrows (i.e., $\sum \mathbf{d}_k = 0$). The D-core (Fig. 1a) resolves each of the \mathbf{d}_k by a DD vector \mathbf{d}'_k (blue arrow) of $\sim \mathbf{b}/3$ along a $\{110\}$ plane and a very small DD (not visible in Fig. 1a). For the ND-cores (Fig. 1b-c), each \mathbf{d}_k is nearly equally compensated by two smaller DD vectors \mathbf{d}''_k (blue arrows) on two equivalent $\{110\}$ planes; each of the smaller DD vector \mathbf{d}''_k is $\sim \mathbf{b}/6$. Formation of the D-/ND-core is determined by the energy cost of the competing structures outside the core

centre: one with a single \mathbf{d}'_k of $\mathbf{b}/3$ and the other with a pair of \mathbf{d}''_k of $\mathbf{b}/6$. The ND-core is thus preferred if the stacking fault energy at $\mathbf{b}/6$ is less than half of that at $\mathbf{b}/3$, in agreement with the proposed γ -line criterion.¹⁸

To verify this suggestion, we determine the relationships between core structures of 7 BCC TMs and γ -lines (Fig. 2a), inter-string energy profiles (Fig. 2b), elastic constants (Fig. 2c), and cohesive energy difference ΔE between the FCC and BCC structure (Fig. 2d). The core structures are calculated with 72 different interatomic potentials covering Group V (V, Nb, Ta), VI (Cr, Mo, W) and VIII (Fe) TMs. The potentials use different forms, including EAM/MEAM,²⁷ Bond-order,¹⁷ machine-learning GAP.²² While the potential accuracies vary, they may be considered as 72 different model elementary metals or average alloys, and thus represent an unbiased examination of the proposed criteria. These potentials yield both D- and ND-cores. However, no correlation is seen between core structures and element types, γ -lines, elastic constants, inter-string energy profiles, or potential formalisms. Instead, the results show that potentials with ΔE above 65% of the pure BCC TMs properties (DFT values) have ND-cores in agreement with first-principle DFT calculations. This governing relation can be captured by the parameter $\chi = \Delta E^A / \Delta E^P$, where ΔE^A is the property of the average alloy (represented here by the various interatomic potentials) and ΔE^P is the intrinsic property of a pure BCC TM (represented here by the more reliable DFT-based calculations). The ND-core is seen for nearly all potentials with $\chi > 0.65$ and D-core is seen when $\chi < 0.45$. This simple criterion is extremely predictive; failing in only 3/72 cases examined (see SI). Near the threshold $0.45 < \chi < 0.65$, both D- and ND-cores are seen, indicating influences of other properties; e.g., elastic constants, or the shapes of the γ -surfaces.

To further validate the above χ -core-transition criterion, we develop two new interatomic potentials for BCC vanadium (V1 and V2). These potentials have nearly identical properties (lattice parameters, elastic constants, surface energies, γ -surfaces, see Extended Data Fig. 4, 5a-b); differing mainly in ΔE^A (V1 and V2 have $\chi = 0.37$ and 0.51). V1 exhibits a D-core and V2

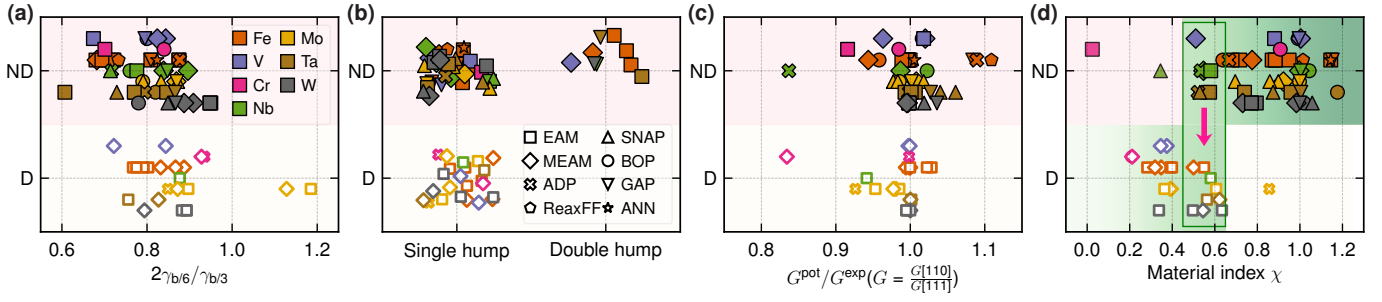


Fig. 2 | Dislocation core structure vs proposed governing criteria. (a) γ -line; (b) shear modulus ratio; (c) inter-string energy profiles and (d) new material index χ . In all figures, the colors and symbols denote different elements and different interatomic interaction forms, respectively. Dislocation cores transform from non-degenerate to degenerate as χ drops below ~ 0.5 .

169 has a ND-core (Extended Data Fig. 5c-d), in agreement with
 170 the χ -core-transition criterion. This criterion thus appears to
 171 be generally applicable. While empirical, it is rooted in a geo-
 172 metric model,²⁵ as illustrated below.

173 On BCC $\{110\}$ planes, the atomic stacking follows an
 174 ABAB sequence, which is similar to the ABAB close pack-
 175 ing on $\{0001\}$ planes of hexagonal close packed (HCP) struc-
 176 tures (Fig. 3a-c). This stacking can be converted to quasi close
 177 packing if atoms on the B-layer are displaced to the centroids
 178 of triangles formed by the A-layer atom triplets (blue dashed
 179 triangle in Fig. 3a). The required displacements are along the
 180 $\langle 110 \rangle$ -direction on $\{110\}$ planes (red arrow in Fig. 3e) and
 181 can be provided by non-screw components of the dislocation
 182 field. Each fractional Burgers vector \mathbf{d}_k has an excess edge
 183 component displacement (EECD, see Methods), but the details
 184 vary between the D- and ND-cores. We illustrate the EECDs
 185 (Fig. 3f-i) in the D-core of Li computed by a new MEAM po-
 186 tential and in the ND-core of W described by an EAM po-
 187 tential.²⁸ In the D-core of Li (Fig. 3f), the EECDs mainly shift 6
 188 atoms (3 at the core centre and 3 in the neighbouring) in $\langle 110 \rangle$
 189 directions on three $\{110\}$ planes. Taking any pair of atoms in
 190 the pink shaded box as an example (Fig. 3f, others have similar
 191 EECDs by symmetry), both atoms have EECDs along $\langle 110 \rangle$.
 192 The EECDs (arrows in Fig. 3f-g) move the two atoms on the
 193 A-layer (yellow atoms in Fig. 3e) towards the centroids of tri-
 194 angles formed by the B-layer atom triplets above them (black
 195 triangle), thus forming a local close packed structure similar
 196 to that in FCC/HCP (*cf.* Fig. 3b,c,e). This displacement also
 197 put these two atoms in the C-layer position with respect to
 198 the A and B layer beneath them, forming a local quasi-ABC
 199 stacking sequence. Kinematically, the EECD leads to similar
 200 differential displacements ($\mathbf{d}_k \approx \mathbf{d}'_k \approx \mathbf{b}/3$) of the two
 201 atoms and hence the D-core structure. Energetically, the re-
 202 sulting close packed, quasi-ABC stacking is favourable at the
 203 core of Li since $\Delta E = -0.8$ meV/Atom. In contrast, the
 204 EECDs of W-EAM-ND (Fig. 3h-i) are relatively small and not
 205 aligned on $\{110\}$ planes. In this case, displacements in the
 206 $\langle 110 \rangle$ directions on $\{110\}$ planes incur a high energy penalty
 207 since the ABC close packed structure is highly unfavourable
 208 ($\Delta E = 470$ meV/atom). Therefore, the D-/ND-core competi-
 209 tion is determined by the energy cost associated with displace-
 210 ments along $\langle 110 \rangle$ on $\{110\}$ planes that lead to close packed
 211 structures. Li and W represent extreme scenarios of the D-
 212 and ND-cores; similar examination of the Fe-GAP-ND²³ core
 213 ($\Delta E = 159$ meV/atom, $\chi = 1.15$) and Fe-MEAM-D²⁹ core
 214 ($\Delta E = 44$ meV/atom, $\chi = 0.32$) shows that their EECDs fall
 215 between these two cases (see Extended Data Fig. 8).

216 The structure formed at the D-core is not precisely FCC,

217 but only similar in close packing sequence; the geometric
 218 model is thus expected to be qualitative. Nevertheless, the
 219 model explains the trend in Fig. 2, where the transition from
 220 ND- to D-core occurs as χ drops below ~ 0.5 (towards smaller
 221 ΔE). Smaller ΔE implies that FCC structure becomes less un-
 222 favourable (relative to BCC) and forming the quasi-ABC struc-
 223 ture is increasingly favourable. Our extensive study of core
 224 structures using different interatomic potentials (Fig. 2) indi-
 225 cates that relating the energy of the quasi-ABC structure to that
 226 of the perfect FCC structure is of sufficient accuracy to distin-
 227 guish between D- and ND-cores. The current model, based on
 228 ΔE , is also consistent with DFT calculations for all BCC TMs
 229 performed to date. For all BCC TMs, ΔE is large (from 138
 230 to 483 meV/atom, Extended Data Fig. 3) and the FCC struc-
 231 tures are highly unfavourable, suggesting limited EECs in
 232 $\langle 110 \rangle$ directions on $\{110\}$ planes. All cores thus prefer the
 233 ND-core structure (Fig. 1b-c and other DFT calculations¹⁵).
 234 On the other hand, alkaline metals have nearly zero ΔE and
 235 show D-cores (Fig. 1a for Li-DFT and Extended Data Fig. 9
 236 for Li, Na and K-interatomic potentials).

237 This analysis rationalises the general model relating core
 238 structure to χ , providing a physical/thermodynamic basis for
 239 understanding core structures in BCC metals. This model
 240 has practical, engineering application for BCC TM alloy de-
 241 sign; since χ depends on the energy difference of two ele-
 242 mentary structures ΔE , alloying can effectively modulate ΔE ,
 243 and thereby manipulate core structure/slip. DFT calculations
 244 can predict χ as a function of solute concentration to identify
 245 favourable solute types/concentrations. We demonstrate this
 246 strategy in binary W-Transition-Metal alloys, a well-studied
 247 system in experiments^{8,11} and simulations.⁷

248 We employ the virtual crystal approximation (VCA) in DFT
 249 to predict χ for alloys. VCA treats alloys using a virtual atom
 250 with a weighted core (pseudopotential) and valence electron
 251 number from the alloy constituents. While the accuracy of
 252 such an approach is limited (*cf.* solute atom substitution in
 253 large supercells), it retains the DFT framework and reasonably
 254 reproduces average, homogeneous alloy properties (see Meth-
 255 ods). Figure 4 shows the predicted χ as a function of solute
 256 concentration c for 28 binary W-alloys. At low solute con-
 257 centrations (< 10 at.%), χ increases for elements to the left of
 258 W in the periodic table and decreases sharply (favourably) for
 259 elements to its right. Increasing solute valence electron con-
 260 centration (VEC³⁰) decreases χ and its slope; this is consistent
 261 with the observation that FCC TM structures predominate on
 262 the right side of the periodic table. The χ -based model identi-
 263 fies solutes capable of ductilizing W that are broadly consistent
 264 with nearly all experiments performed to date.¹² For W-Re al-

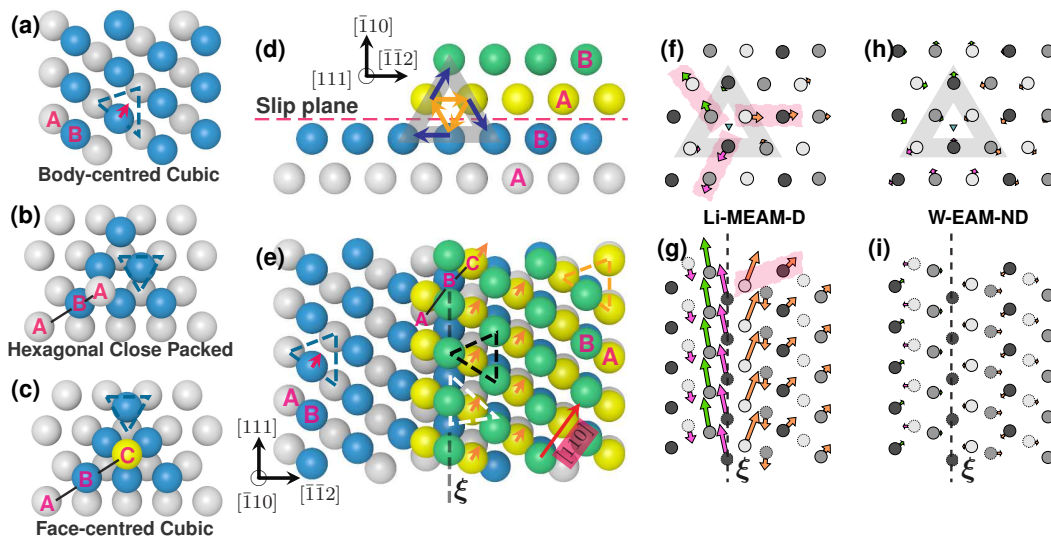


Fig. 3 | Atomic stacking orders of BCC, HCP and FCC structures and EECDs of screw dislocations. (a-c) Atomic stacking of BCC $\{110\}$, HCP $\{0001\}$ and FCC $\{111\}$ planes. (d-e) Atomic structure of the screw dislocation core viewed in two directions. Displacements of atoms on the second A-layer in the $[110]$ direction on the $(\bar{1}\bar{1}0)$ plane (orange arrows) creates a quasi-ABC stacking, similar to that in the FCC structure. (f-i) EECDs (arrows) in cores of Li-MEAM and W-EAM.

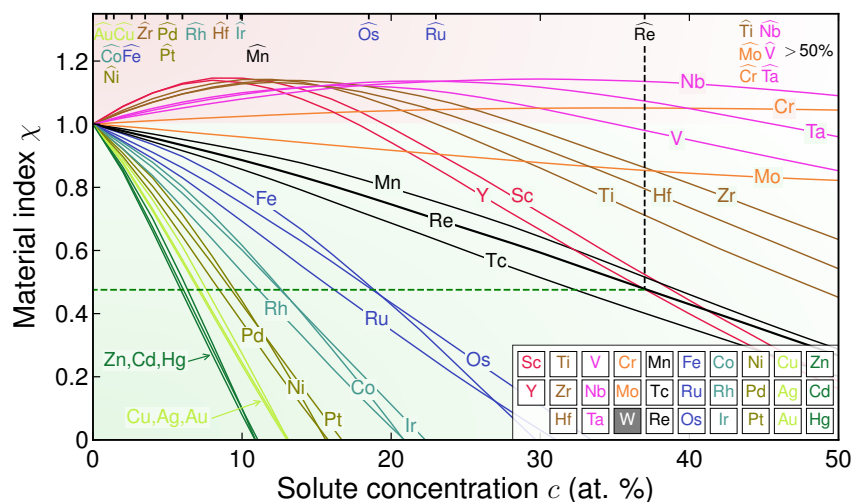


Fig. 4 | Prediction of material index χ as a function of solute concentrations for binary W-TM alloys from VCA DFT calculations. Lower χ favours the non-degenerate core. Solute elements below the Re line have better effects. The solubility of each element in W is denoted by the $\hat{}$ symbol at the top. The elements are colour-coded by Group in the periodic table.

265 loys, in particular, the VCA data show that χ decreases with
 266 increasing Re content at all concentrations; reducing to 0.6 at
 267 30at.%Re. This Re concentration is close to many commer-
 268 cial W-Re alloys exhibiting high ductility and a DBT below
 269 room temperature. Transformations from the ND- to D-core
 270 in W-Re alloys were also demonstrated in early DFT calcula-
 271 tions^{7,8} at 25at.%Re, in agreement with the VCA and χ model
 272 predictions. For W-Ta alloys, no transformation is predicted,
 273 in agreement with DFT calculations⁸ and experiments where
 274 $\{112\}$ slip is not seen.⁸ While the VCA calculation in Fig. 4
 275 finds many solutes (Tc, Fe, Os, Ru, Rh, Co, Ir etc.) better than
 276 Re in ductilizing W, their practical application is limited by
 277 solubility³¹ and/or cost. Re is thus one of the most practical
 278 solutes for ductilizing W. The present predictions provide ex-
 279 plicit recommendations of solutes and concentrations that may
 280 be explored through nonequilibrium techniques (e.g., mechan-
 281 ical alloying or plasma sintering) to overcome solubility limits.

282 Change from the ND-core to D-core can have multiple ef-
 283 fects on dislocation behaviour and material plasticity; the most

284 important of which is the activation of additional slip systems.
 285 D-core screw dislocations tend to slip on $\{112\}$ planes, while
 286 ND-core on $\{110\}$ planes.² In alloys, both D- and ND-core
 287 dislocations can co-exist, depending on local solute concentra-
 288 tions. Their co-existence activates 24 slip systems; i.e., twice
 289 the number of ND-core-favoured $\{110\}$ slips. The importance
 290 of a drastic increase in the number of available slip systems
 291 cannot be underestimated, as is well-known in non-cubic sys-
 292 tems.² At low temperatures, pure BCC TMs tend to be brittle;
 293 largely because slip is inhibited by high lattice friction and
 294 limited to $\{110\}$ systems. With increasing temperature, the
 295 ductility of these pure TMs enhance drastically as lattice fric-
 296 tion is reduced and additional slip planes ($\{112\}$ and $\{123\}$)
 297 are thermally activated. The effect of thermal activation can
 298 be equivalently achieved by solutes via core structure change.
 299 Plastic deformation of alloys with ductilizing solutes (e.g., Re
 300 in W) at lower temperatures can thus be similar to that of pure
 301 TMs at higher temperatures. This suggests that favourable so-
 302 lutes can lower the DBT temperatures, as seen in Re-W alloys.

The ductility of W also depends on crystal orientation (texture) and grain size;³² single crystals are generally ductile and polycrystals brittle. This further demonstrates that activation of additional slip systems can be critical; providing the flexibility required for strain compatibility at grain boundaries and junctions and reducing texture-dependence in structural alloys.

Solute atoms can also increase or decrease lattice friction by modifying double-kink nucleation/propagation, dislocation cross-slip and interactions. These local effects vary between BCC TMs and should not be overlooked. Nevertheless, since the index χ is built upon crystal geometry and bonding characteristics (as captured by the energy difference of two simple crystal structures), and is validated across nearly all interatomic potentials available, we suggest that the approach presented here is general and the alloying effects seen here in W will be replicated in other BCC TMs (e.g., Fe/Nb alloys).

In summary, we presented a general model with a new material index χ for predicting the nature of screw dislocation core structure in all BCC materials. The χ -model rationalises core structures in pure alkaline metals, BCC TMs and their alloys. More importantly, χ can be computed rapidly for any alloy composition using DFT, providing a practical computational approach for ductile and tough BCC TM alloy design. This new approach is tested in the W-based binary system and correctly identifies Re as the most practical solute for ductilizing W alloys (and the appropriate Re concentration range). The material index χ does not predict ductility or toughness directly (influenced by metallurgic processing routes) but does, nevertheless, provide a fundamental constraint on the nature of plasticity in these materials. The proposed χ approach is first-principles-based; hence it is applicable to a wide-range of complex alloys where ductility is controlled/limited by nature's choice of slip systems.

References

References 1-33 are for the main text.

* Corresponding author: zhaoxuwu@cityu.edu.hk

- [1] P. Gumbsch, J. Riedle, A. Hartmaier, and H. F. Fischmeister, Controlling factors for the brittle-to-ductile transition in tungsten single crystals, *Science* **282**, 1293 (1998).
- [2] V. Vitek and V. Paidar, Non-planar dislocation cores: A ubiquitous phenomenon affecting mechanical properties of crystalline materials, in *Dislocations in Solids*, Vol. 14, edited by J. P. Hirth (Elsevier, 2008) Chap. 87, pp. 439–514.
- [3] L. Proville, D. Rodney, and M.-C. Marinica, Quantum effect on thermally activated glide of dislocations, *Nature Materials* **11**, 845 (2012).
- [4] P. Gumbsch, Brittle fracture and the brittle-to-ductile transition of tungsten, *J. Nucl. Mater.* **323**, 304 (2003).
- [5] D. Rodney, L. Ventelon, E. Clouet, L. Pizzagalli, and F. Willaime, Ab initio modeling of dislocation core properties in metals and semiconductors, *Acta Mater.* **124**, 633 (2017).
- [6] P. Schade, 100 years of doped tungsten wire, *Int. J. Refract. Met. Hard Mat.* **28**, 648 (2010).
- [7] L. Romaner, C. Ambrosch-Draxl, and R. Pippan, Effect of rhenium on the dislocation core structure in tungsten, *Phys. Rev. Lett.* **104**, 195503 (2010).
- [8] H. Li, S. Wurster, C. Motz, L. Romaner, C. Ambrosch-Draxl, and R. Pippan, Dislocation-core symmetry and slip planes in tungsten alloys: Ab initio calculations and microcantilever bending experiments, *Acta Mater.* **60**, 748 (2012).
- [9] T. Joseph, M. Tanaka, A. Wilkinson, and S. Roberts, Brittle-ductile transitions in vanadium and iron–chromium, *J. Nucl. Mater.* **367-370**, 637 (2007).
- [10] B. G. Butler, J. D. Paramore, J. P. Ligda, C. Ren, Z. Z. Fang, S. C. Middlemas, and K. J. Hemker, Mechanisms of deformation and ductility in tungsten – a review, *Int. J. Refract. Met. Hard Mat.* **75**, 248 (2018).
- [11] J. R. Stephens, Dislocation structures in single-crystal tungsten and tungsten alloys, *Metall. Mater. Trans. B* **1**, 1293 (1970).
- [12] C. Ren, Z. Fang, M. Koopman, B. Butler, J. Paramore, and S. Middlemas, Methods for improving ductility of tungsten – A review, *Int. J. Refract. Met. Hard Mat.* **75**, 170 (2018).
- [13] E. Clouet, L. Ventelon, and F. Willaime, Dislocation core energies and core fields from first principles, *Phys. Rev. Lett.* **102**, 055502 (2009).
- [14] C. R. Weinberger, B. L. Boyce, and C. C. Battaile, Slip planes in bcc transition metals, *Int. Mater. Rev.* **58**, 296 (2013).
- [15] L. Dezerald, L. Ventelon, E. Clouet, C. Denoual, D. Rodney, and F. Willaime, Ab initio modeling of the two-dimensional energy landscape of screw dislocations in bcc transition metals, *Phys. Rev. B* **89**, 024104 (2014).
- [16] R. Gröger and V. Vitek, Directional versus central-force bonding in studies of the structure and glide of $1/2\langle 111 \rangle$ screw dislocations in bcc transition metals, *Philos. Mag.* **89**, 3163 (2009).
- [17] Y.-S. Lin, M. Mrovec, and V. Vitek, A new method for development of bond-order potentials for transition bcc metals, *Model. Simul. Mater. Sci. Eng.* **22**, 034002 (2014).
- [18] M. Duesbery and V. Vitek, Plastic anisotropy in b.c.c. transition metals, *Acta Mater.* **46**, 1481 (1998).
- [19] M. R. Fellingner, H. Park, and J. W. Wilkins, Force-matched embedded-atom method potential for niobium, *Phys. Rev. B* **81**, 144119 (2010).
- [20] M. Mrovec, D. Nguyen-Manh, D. G. Pettifor, and V. Vitek, Bond-order potential for molybdenum: Application to dislocation behavior, *Phys. Rev. B* **69**, 094115 (2004).
- [21] S. Chiesa, M. Gilbert, S. Dudarev, P. Derlet, and H. V. Swygenhoven, The non-degenerate core structure of a $1/2\langle 111 \rangle$ screw dislocation in bcc transition metals modelled using Finnis–Sinclair potentials: The necessary and sufficient conditions, *Philos. Mag.* **89**, 3235 (2009).
- [22] A. P. Bartók, M. C. Payne, R. Kondor, and G. Csányi, Gaussian approximation potentials: The accuracy of quantum mechanics, without the electrons, *Phys. Rev. Lett.* **104**, 136403 (2010).
- [23] D. Dragoni, T. D. Daff, G. Csányi, and N. Marzari, Achieving DFT accuracy with a machine-learning interatomic potential: Thermomechanics and defects in bcc ferromagnetic iron, *Phys. Rev. Mater.* **2**, 013808 (2018).
- [24] F. Maresca, D. Dragoni, G. Csányi, N. Marzari, and W. A. Curtin, Screw dislocation structure and mobility in body centered cubic Fe predicted by a gaussian approximation potential, *npj Comput. Mater.* **4**, 69 (2018).
- [25] F. Kroupa and V. Vitek, Splitting of dislocations in b.c.c. metals on $\{110\}$ planes, *Czechoslovak Journal of Physics* **14**, 337 (1964).
- [26] P. M. Anderson, J. P. Hirth, and J. Lothe, *Theory of Dislocations* (Cambridge University Press, 2017).
- [27] M. I. Baskes, Modified embedded-atom potentials for cubic materials and impurities, *Phys. Rev. B* **46**, 2727 (1992).
- [28] W. Setyawan, N. Gao, and R. J. Kurtz, A tungsten-rhenium interatomic potential for point defect studies, *J. Appl. Phys.* **123**, 205102 (2018).
- [29] E. Asadi, M. A. Zaem, S. Nouranian, and M. I. Baskes, Quantitative modeling of the equilibration of two-phase solid-liquid Fe by atomistic simulations on diffusive time scales, *Phys. Rev. B* **91**, 024105 (2015).
- [30] S. Guo, C. Ng, J. Lu, and C. T. Liu, Effect of valence electron concentration on stability of fcc or bcc phase in high entropy alloys, *J. Appl. Phys.* **109**, 103505 (2011).
- [31] T. B. Massalski, H. Okamoto, P. Subramanian, and L. Kacprzak, *Binary Alloy Phase Diagrams*, 2nd ed. (Materials Park, Ohio, ASM International, 1990).
- [32] Y. Zhang, A. V. Ganeev, J. T. Wang, J. Q. Liu, and I. V. Alexandrov, Observations on the ductile-to-brittle transition in ultrafine-grained tungsten of commercial purity, *Mater. Sci. Eng. A* **503**, 37 (2009).
- [33] G. Kresse and J. Furthmüller, Efficient iterative schemes for *ab initio* total-energy calculations using a plane-wave basis set,

- Phys. Rev. B **54**, 11169 (1996).
- [34] G. Kresse and D. Joubert, From ultrasoft pseudopotentials to the projector augmented-wave method, *Phys. Rev. B* **59**, 1758 (1999).
- [35] J. P. Perdew, K. Burke, and M. Ernzerhof, Generalized gradient approximation made simple, *Phys. Rev. Lett.* **77**, 3865 (1996).
- [36] P. E. Blöchl, Projector augmented-wave method, *Phys. Rev. B* **50**, 17953 (1994).
- [37] M. Methfessel and A. T. Paxton, High-precision sampling for Brillouin-zone integration in metals, *Phys. Rev. B* **40**, 3616 (1989).
- [38] H. J. Monkhorst and J. D. Pack, Special points for Brillouin-zone integrations, *Phys. Rev. B* **13**, 5188 (1976).
- [39] S. Plimpton, Fast parallel algorithms for short-range molecular dynamics, *Journal of Computational Physics* **117**, 1 (1995).
- [40] A. P. Bartók, R. Kondor, and G. Csányi, On representing chemical environments, *Phys. Rev. B* **87**, 184115 (2013).
- [41] A. P. Bartók and G. Csányi, *International Journal of Quantum Chemistry*.
- [42] This software is available for non-commercial use from www.libatoms.org.
- [43] C. A. Becker, F. Tavazza, Z. T. Trautt, and R. A. B. de Macedo, Considerations for choosing and using force fields and interatomic potentials in materials science and engineering, *Current Opinion in Solid State and Materials Science* **17**, 277 (2013).
- [44] E. B. Tadmor, R. S. Elliott, J. P. Sethna, R. E. Miller, and C. A. Becker, The potential of atomistic simulations and the knowledgebase of interatomic models, *JOM* **63**, 17 (2011).
- [45] V. Vitek, Intrinsic stacking faults in body-centred cubic crystals, *Philos. Mag.* **18**, 773 (1968).
- [46] J. A. Nieminen, A. P. Sutton, and J. B. Pethica, Static junction growth during frictional sliding of metals, *Acta Metall. et Materialia* **40**, 2503 (1992).
- [47] S. Kibey, J. B. Liu, D. D. Johnson, and H. Sehitoglu, Generalized planar fault energies and twinning in Cu–Al alloys, *Applied Physics Letters* **89**, 191911 (2006).
- [48] B. Yin, Z. Wu, and W. A. Curtin, Comprehensive first-principles study of stable stacking faults in hcp metals, *Acta Mater.* **123**, 223 (2017).
- [49] V. Bulatov and W. Cai, *Computer Simulations of Dislocations* (Oxford University Press, USA, 2006).
- [50] X.-G. Li, C. Chen, H. Zheng, Y. Zuo, and S. P. Ong, Complex strengthening mechanisms in the NbMoTaW multi-principal element alloy, *npj Comput. Mater.* **6**, 70 (2020).
- [51] M. I. Mendeleev, S. Han, D. J. Srolovitz, G. J. Ackland, D. Y. Sun, and M. Asta, Development of new interatomic potentials appropriate for crystalline and liquid iron, *Philos. Mag.* **83**, 3977 (2003).
- [52] V. Vitek, R. C. Perrin, and D. K. Bowen, The core structure of $\frac{1}{2}(111)$ screw dislocations in b.c.c. crystals, *Philos. Mag. A* **21**, 1049 (1970).
- [53] A. Stukowski, Visualization and analysis of atomistic simulation data with OVITO—the Open Visualization Tool, *Model. Simul. Mater. Sci. Eng. Engineering* **18**, 015012 (2009).
- [54] L. Bellaiche and D. Vanderbilt, Virtual crystal approximation revisited: Application to dielectric and piezoelectric properties of perovskites, *Phys. Rev. B* **61**, 7877 (2000).
- [55] P. Giannozzi, S. Baroni, N. Bonini, M. Calandra, R. Car, C. Cavazzoni, D. Ceresoli, G. L. Chiarotti, M. Cococcioni, I. Dabo, A. D. Corso, S. de Gironcoli, S. Fabris, G. Fratesi, R. Gebauer, U. Gerstmann, C. Gougoussis, A. Kokalj, M. Lazzeri, L. Martin-Samos, N. Marzari, F. Mauri, R. Mazzarello, S. Paolini, A. Pasquarello, L. Paulatto, C. Sbraccia, S. Scandolo, G. Sclauzero, A. P. Seitsonen, A. Smogunov, P. Umari, and R. M. Wentzcovitch, QUANTUM ESPRESSO: a modular and open-source software project for quantum simulations of materials, *J. Condens. Matter Phys.* **21**, 395502 (2009).
- [56] D. Vanderbilt, Soft self-consistent pseudopotentials in a generalized eigenvalue formalism, *Phys. Rev. B* **41**, 7892 (1990).
- [57] A. M. Rappe, K. M. Rabe, E. Kaxiras, and J. D. Joannopoulos, Optimized pseudopotentials, *Phys. Rev. B* **41**, 1227 (1990).
- [58] A. Dal Corso, Pseudopotentials periodic table: From H to Pu, *Comput. Mater. Sci.* **95**, 337 (2014).
- [59] N. Marzari, D. Vanderbilt, A. De Vita, and M. C. Payne, Thermal contraction and disordering of the Al(110) surface, *Phys. Rev. Lett.* **82**, 3296 (1999).
- [60] Y. Zuo, C. Chen, X. Li, Z. Deng, Y. Chen, J. Behler, G. Csányi, A. V. Shapeev, A. P. Thompson, M. A. Wood, and et al., Performance and cost assessment of machine learning interatomic potentials, *The Journal of Physical Chemistry A* **124**, 731 (2020).
- [61] M. Alam and S. Groh, Dislocation modeling in bcc lithium: A comparison between continuum and atomistic predictions in the modified embedded atoms method, *Journal of Physics and Chemistry of Solids* **82**, 1 (2015).
- [62] S. Groh and M. Alam, Fracture behavior of lithium single crystal in the framework of (semi-)empirical force field derived from first-principles, *Model. Simul. Mater. Sci. Eng. Engineering* **23**, 045008 (2015).
- [63] X. Zhou, LAMMPS EIM potential for the Br-Cl-Cs-F-I-K-Li-Na-Rb system (2010).
- [64] M. I. Mendeleev, S. Han, W.-J. Son, G. J. Ackland, and D. J., Srolovitz, Simulation of the interaction between Fe impurities and point defects in V, *Phys. Rev. B* **76**, 214105 (2007).
- [65] B.-J. Lee, M. I. Baskes, H. Kim, and Y. Koo Cho, Second nearest-neighbor modified embedded atom method potentials for bcc transition metals, *Phys. Rev. B* **64**, 184102 (2001).
- [66] S. B. Maisel, W.-S. Ko, J.-L. Zhang, B. Grabowski, and J. Neugebauer, Thermomechanical response of NiTi shape-memory nanoprecipitates in TiV alloys, *Phys. Rev. Mater.* **1**, 033610 (2017).
- [67] Y.-S. Lin, M. Mrovec, and V. Vitek, A new method for development of bond-order potentials for transition bcc metals, *Model. Simul. Mater. Sci. Eng. Engineering* **22**, 034002 (2014).
- [68] J. Byggmästar, K. Nordlund, and F. Djurabekova, Gaussian approximation potentials for body-centered-cubic transition metals, *Phys. Rev. Mater.* **4**, 093802 (2020).
- [69] Y. Zhang, R. Ashcraft, M. Mendeleev, C. Z. Wang, and K. F. Kelton, Experimental and molecular dynamics simulation study of structure of liquid and amorphous Ni₆₂Nb₃₈ alloy, *The Journal of Chemical Physics* **145**, 204505 (2016).
- [70] C. Yang and L. Qi, Modified embedded-atom method potential of niobium for studies on mechanical properties, *Comput. Mater. Sci.* **161**, 351 (2019).
- [71] D. Smirnova and S. Starikov, An interatomic potential for simulation of Zr-Nb system, *Comput. Mater. Sci.* **129**, 259 (2017).
- [72] R. Ravelo, T. C. Germann, O. Guerrero, Q. An, and B. L. Holian, Shock-induced plasticity in tantalum single crystals: Interatomic potentials and large-scale molecular-dynamics simulations, *Phys. Rev. B* **88**, 134101 (2013).
- [73] Y. Li, D. J. Siegel, J. B. Adams, and X.-Y. Liu, Embedded-atom-method tantalum potential developed by the force-matching method, *Phys. Rev. B* **67**, 125101 (2003).
- [74] X. W. Zhou, H. N. G. Wadley, J. S. Filhol, and M. N. Neurock, Modified charge transfer–embedded atom method potential for metal/metal oxide systems, *Phys. Rev. B* **69**, 035402 (2004).
- [75] Y. Chen, J. Fang, L. Liu, W. Hu, N. Gao, F. Gao, and H. Deng, Development of the interatomic potentials for W-Ta system, *Comput. Mater. Sci.* **163**, 91 (2019).
- [76] G. P. Pun, K. Darling, L. Kecskes, and Y. Mishin, Angular-dependent interatomic potential for the Cu–Ta system and its application to structural stability of nano-crystalline alloys, *Acta Mater.* **100**, 377 (2015).
- [77] A. P. Thompson, L. P. Swiler, C. R. Trott, S. M. Foiles, and G. J. Tucker, Spectral neighbor analysis method for automated generation of quantum-accurate interatomic potentials, *Journal of Computational Physics* **285**, 316 (2015).
- [78] M. Mendeleev, Finnis-Sinclair potential for the Fe-Ni-Cr system developed by Mendeleev et al. (2020) v000, OpenKIM [10.25950/538764D4](https://openkim.org/item/10.25950/538764D4) (2020).
- [79] W.-M. Choi, Y. Kim, D. Seol, and B.-J. Lee, Modified embedded-atom method interatomic potentials for the Co-Cr, Co-Fe, Co-Mn, Cr-Mn and Mn-Ni binary systems, *Comput. Mater. Sci.* **130**, 121 (2017).

- [80] C. A. Howells and Y. Mishin, Angular-dependent interatomic potential for the binary Ni–Cr system, *Model. Simul. Mater. Sci. Eng.* **26**, 085008 (2018).
- [81] G. J. Ackland, G. Tichy, V. Vitek, and M. W. Finnis, Simple N-body potentials for the noble metals and nickel, *Philos. Mag. A* **56**, 735 (1987).
- [82] H. Park, M. R. Fellingner, T. J. Lenosky, W. W. Tipton, D. R. Trinkle, S. P. Rudin, C. Woodward, J. W. Wilkins, and R. G. Hennig, *Ab initio* based empirical potential used to study the mechanical properties of molybdenum, *Phys. Rev. B* **85**, 214121 (2012).
- [83] J.-S. Kim, D. Seol, J. Ji, H.-S. Jang, Y. Kim, and B.-J. Lee, Second nearest-neighbor modified embedded-atom method interatomic potentials for the Pt-M (M = Al, Co, Cu, Mo, Ni, Ti, V) binary systems, *Calphad* **59**, 131 (2017).
- [84] S. Starikov, L. Kolotova, A. Kuksin, D. Smirnova, and V. Tseplyaev, Atomistic simulation of cubic and tetragonal phases of U-Mo alloy: Structure and thermodynamic properties, *J. Nucl. Mater.* **499**, 451 (2018).
- [85] C. Chen, Z. Deng, R. Tran, H. Tang, I.-H. Chu, and S. P. Ong, Accurate force field for molybdenum by machine learning large materials data, *Phys. Rev. Mater.* **1**, 043603 (2017).
- [86] P. A. Olsson, Semi-empirical atomistic study of point defect properties in BCC transition metals, *Comput. Mater. Sci.* **47**, 135 (2009).
- [87] M.-C. Marinica, L. Ventelon, M. R. Gilbert, L. Proville, S. L. Dudarev, J. Marian, G. Bencteux, and F. Willaime, Interatomic potentials for modelling radiation defects and dislocations in tungsten, *J. Condens. Matter Phys.* **25**, 395502 (2013).
- [88] G. Bonny, A. Bakaev, D. Terentyev, and Y. A. Mastrikov, Interatomic potential to study plastic deformation in tungsten-rhenium alloys, *J. Appl. Phys.* **121**, 165107 (2017).
- [89] Ellad Tadmor, LAMMPS MEAM Potential for W developed by Lenosky (2017) v000, OpenKIM [10.25950/264A7B3E](https://openkim.org/item/10.25950/264A7B3E) (2019).
- [90] H. Park, M. Fellingner, T. Lenosky, W. Tipton, D. Trinkle, S. P. Rudin, C. Woodward, J. Wilkins, and R. Hennig, MEAM potential for W developed by Park et al. (2012) v001 [10.25950/A4A622CF](https://openkim.org/item/10.25950/A4A622CF) (2021).
- [91] J. R. Morris, R. S. Aga, V. Levashov, and T. Egami, Many-body effects in bcc metals: An embedded atom model extension of the modified johnson pair potential for iron, *Phys. Rev. B* **77**, 174201 (2008).
- [92] G. Bonny, R. C. Pasianot, and L. Malerba, Fitting interatomic potentials consistent with thermodynamics: Fe, Cu, Ni and their alloys, *Philos. Mag.* **89**, 3451 (2009).
- [93] S. Chiesa, P. M. Derlet, S. L. Dudarev, and H. V. Swygenhoven, Optimization of the magnetic potential for α -Fe, *J. Condens. Matter Phys.* **23**, 206001 (2011).
- [94] H. Chamati, N. Papanicolaou, Y. Mishin, and D. Papaconstantopoulos, Embedded-atom potential for Fe and its application to self-diffusion on Fe(100), *Surf. Sci.* **600**, 1793 (2006).
- [95] R. Meyer and P. Entel, Martensite-austenite transition and phonon dispersion curves of $\text{Fe}_{1-x}\text{Ni}_x$ studied by molecular-dynamics simulations, *Phys. Rev. B* **57**, 5140 (1998).
- [96] G. J. Ackland, D. J. Bacon, A. F. Calder, and T. Harry, Computer simulation of point defect properties in dilute Fe–Cu alloy using a many-body interatomic potential, *Philos. Mag. A* **75**, 713 (1997).
- [97] L. Malerba, M. Marinica, N. Anento, C. Björkas, H. Nguyen, C. Domain, F. Djurabekova, P. Olsson, K. Nordlund, A. Serra, D. Terentyev, F. Willaime, and C. Becquart, Comparison of empirical interatomic potentials for iron applied to radiation damage studies, *J. Nucl. Mater.* **406**, 19 (2010).
- [98] S. Starikov, D. Smirnova, T. Pradhan, Y. Lysogorskiy, H. Chapman, M. Mrovec, and R. Drautz, Angular-dependent interatomic potential for large-scale atomistic simulation of iron: Development and comprehensive comparison with existing interatomic models, *Phys. Rev. Mater.* **5**, 063607 (2021).
- [99] H.-K. Kim, W.-S. Jung, and B.-J. Lee, Modified embedded-atom method interatomic potentials for the Fe–Ti–C and Fe–Ti–N ternary systems, *Acta Mater.* **57**, 3140 (2009).
- [100] L. S. I. Liyanage, S.-G. Kim, J. Houze, S. Kim, M. A. Tschopp, M. I. Baskes, and M. F. Horstemeyer, Structural, elastic, and thermal properties of cementite (Fe_3C) calculated using a modified embedded atom method, *Phys. Rev. B* **89**, 094102 (2014).
- [101] J. Byggmästar and F. Granberg, Dynamical stability of radiation-induced C15 clusters in iron, *J. Nucl. Mater.* **528**, 151893 (2020).
- [102] J. Byggmästar and F. Granberg, Dynamical stability of radiation-induced C15 clusters in iron, *J. Nucl. Mater.* **528**, 151893 (2020).
- [103] H. Mori and T. Ozaki, Neural network atomic potential to investigate the dislocation dynamics in bcc iron, *Phys. Rev. Mater.* **4**, 040601 (2020).
- [104] J. Cohen, R. Hinton, K. Lay, and S. Sass, Partial dislocations on the $\{110\}$ planes in the b.c.c. lattice, *Acta Metall.* **10**, 894 (1962).
- [105] V. Vitek and F. Kroupa, Sessile splitting of screw dislocations in b.c.c. metals, *Czechoslovak J. Phys.* **18**, 464 (1968).

Methods

Density-functional calculations

First-principles calculations are performed within the density-functional theory (DFT) framework using the Vienna Ab initio Simulation Package (VASP^{33,34}). The exchange and correlation functional is described by the generalized gradient approximation (GGA) with the Perdew-Burke-Ernzerhof (PBE³⁵) parameterization. The core electrons are replaced by the projector augmented wave (PAW³⁶) pseudopotentials with the valence states shown in Extended Data Table 2. A first-order Methfessel-Paxton method³⁷ is used to smooth eigenstate occupancy. Plane-wave cutoff energy, Γ -centered Monkhorst-Pack k-point sampling mesh³⁸ and the smearing parameters sigma are established through convergence tests of 2 atom BCC unit cells with a threshold energy $\Delta E < 1$ meV/atom. The parameters are shown in Extended Data Table 2.

Two-atom BCC and 4-atom FCC unit cells are used to calculate the energy difference ΔE . In the energy difference and γ -surface calculations, convergence is assumed when energy variation drops below 10^{-5} eV per electronic step and 10^{-4} eV per ionic step. The final ΔE results are shown in Extended Data Table 3. Screw dislocation core structures were optimized until the ionic force is $< 5 \times 10^{-3}$ eV/Å.

Molecular dynamics/statics simulations

Molecular dynamics and static relaxation simulations are performed using the Large-scale Atomic/Molecular Massively Parallel Simulator (LAMMPS³⁹). Structure optimization is performed using the conjugate gradient method. Convergence is assumed when forces on all atoms drop below 10^{-12} eV/Å in calculations of γ surfaces and 10^{-10} eV/Å in calculations of dislocation core structures. For the GAP potential for Fe,^{22,23,40-42} convergence tolerance is relaxed to 10^{-12} eV for energy variation and 10^{-6} eV/Å for atomic forces, due to its high computational cost.

Interatomic Potential Models for BCC Metals

Elementary BCC transition metals have been extensively studied using DFT calculations. A rich set of interatomic potentials have also been developed using various formalisms. In this work, we examined nearly all interatomic potentials (publically accessible) for BCC metals developed up to date. These potentials are available from the National Institute of Standards and Technology (NIST) potential repository,⁴³ the Open Knowledgebase of Interatomic Models (OpenKIM) project⁴⁴ or literature. In total, we examined 72 potentials, as shown in Extended Data Table 1. These potentials use different functional forms in their descriptions of interatomic interactions. The choice made here are not biased toward any particular form or fitting procedures.

In addition, we developed two new MEAM potentials for BCC V (V1 and V2). The potential parameters are fitted using the particle swarm optimization algorithm. These potentials have nearly identical properties (Extended Data Fig. 4), except for ΔE , which is purposely controlled at 91 meV/atom and 124 meV/atom, respectively. With ΔE from DFT at 243 meV/atom, V1 and V2 have $\chi = 0.37$ and 0.51, respectively. V1 adopts a ND-core and V2 adopts a D-core for the screw

dislocation. A new MEAM interatomic potential for Li is also developed with $\Delta E = -0.8$ meV/atom close to that from DFT. All potential parameters are shown in Extended Data Table 4 and can be used in LAMMPS directly.

Calculations of γ surface

The generalized stacking fault energy surfaces (γ -surface) of Li, Ta and W are calculated using DFT. A slab supercell model is used, with its crystal orientation shown in Extended Data Fig. 1d. The slab contains 12 $\{110\}$ -plane atom layers and a 20 Å vacuum layer. γ -surfaces are calculated using the classical method by Vitek.⁴⁵ For each specific stacking fault position, a homogeneous slip displacement in the $\{110\}$ plane is applied to atoms in the upper half block of the supercell to create the stacking fault between the sheared and un-sheared atom block. Stacking fault energies are calculated with all atoms allowed to move in the direction perpendicular to the slip, $\{110\}$ plane.

In the calculations of γ -surface using interatomic potentials in LAMMPS, tilted supercells of dimensions $\sim 10 \times 10 \times 40$ (Å³) are used. The stacking fault energies are calculated with atoms constrained to move in the direction perpendicular to the slip plane only (same as in DFT, see Refs.⁴⁶⁻⁴⁸ for details).

Calculations of dislocation core structure

Dislocation core structures are calculated using both a dipole configuration (dipole method) and a single dislocation with fixed boundary conditions (cluster method). In the dipole method, a fully periodic prism supercell is chosen with the dislocations arranged in triangular positions, as shown in Extended Data Fig. 1b. The supercell vectors are $(\mathbf{c}_1, \mathbf{c}_2, \mathbf{c}_3 = (1/2[111], n[11\bar{2}], n[\bar{1}2\bar{1}])$. In the DFT calculations, we use $n = 6$, resulting in 324 atoms in the supercell. To fulfill the $\langle 110 \rangle$ -diad and $\langle 111 \rangle$ threefold symmetry of the BCC lattice, the dipole cores have to be placed at the hard-core and easy-core positions, respectively (Extended Data Fig. 1c). The distance between dislocations in the dipole is $6\sqrt{2}a$, where a is the lattice parameter of the BCC lattice. The dipole (a pair of dislocation with opposite Burgers vector $\pm \mathbf{b}$) is introduced using the Babel package developed by E. Clouet. In particular, the displacement field of arrays of dipoles (repeated 16 times in the \mathbf{c}_2 and \mathbf{c}_3 directions) is first applied to atoms in the supercell, followed by applying a homogeneous strain to accommodate the plastic strain introduced by the dipole (see Refs.^{5,13,49} for details). During structure optimization, the cell vectors are always fixed. In DFT calculations, the hard core is meta stable and all atoms are allowed to move. The hard-core is unstable in some interatomic potentials, and atoms near the hard core are fixed, to keep the strict symmetry of the BCC lattice.

The dipole approach uses a fully periodic supercell. It avoids the complexity of free surfaces, but introduces dislocation interactions and a non-negligible homogeneous strain scaling with supercell sizes. Therefore, we also used a hexagonal prism supercell (Extended Data Fig. 1a) with a single dislocation and calculated larger supercells with interatomic potentials. In this approach, supercells of radius $R \sim 92$ Å and length of one Burgers vector are first created in the perfect BCC structures. The crystallographic $\langle 11\bar{2} \rangle$ direction is aligned with the x-axis, $\langle \bar{1}10 \rangle$ aligned with the y-axis and the screw dislocation

line direction $\langle 111 \rangle$ aligned with the z -axis, i.e., the hexagonal prism axis (Fig. 1d). The z -direction has periodic boundary conditions while the x and y directions contain free surfaces. This geometry keeps the $\langle 111 \rangle$ -axis threefold symmetry of the BCC lattice. Each supercell contains ~ 3600 atoms (depending on the element type). A single dislocation is then introduced by displacing atoms according to the anisotropic elastic displacement field of the corresponding Volterra dislocation at the supercell center (easy-core position). Atoms within $\sim 12 \text{ \AA}$ from the outer surface (gray area in Fig. 1a) are always fixed to their elastic displacements. The initial dislocation structure is first optimized using conjugate gradient algorithm at 0 K, then equilibrated for 100,000 steps at finite temperatures (~ 50 K) and optimized again at 0 K. This procedure is not always needed, but helps to obtain well-equilibrated core structures in some interatomic potentials. Only 0 K structure optimization is performed for the GAP potential for Fe.²³ The obtained core structures are summarized in Fig. 2.

Calculations of inter-string interaction energy

The inter-string interaction energy captures energy variation during atomic displacement similar to that in the core center of the screw dislocation, i.e., displacement in the screw dislocation Burgers vector $\langle 111 \rangle$ direction.^{8,21} In DFT, we first construct a fully periodic supercell (24 atoms) with supercell vectors $(\mathbf{c}_1, \mathbf{c}_2, \mathbf{c}_3) = ([11\bar{2}], 2[\bar{1}10], [111])$, as shown in Extended Data Fig. 6. The supercell used in molecular static calculations has the same orientation, but larger size (144 atoms) with supercell vectors $\mathbf{c}_1, \mathbf{c}_2, \mathbf{c}_3 = (2[11\bar{2}], 3[\bar{1}10], 2[111])$. The inter-string interaction energy is calculated by choosing a single column of atoms aligned in the z -axis ($\langle 111 \rangle$ direction) (Extended Data Fig. 6a) and displacing them in the same direction, while other atoms are fixed. The energy variations for Fe, Ta and W are shown in Extended Data Fig. 6b. DFT results show a double-hump in Fe and W, while a single-hump is seen in Ta, suggesting no clear trend in the shape of inter-string interaction potential among the transition metals. In contrast, Fe-GAP,²³ Ta-SNAP⁵⁰ and W-EAM²⁸ have a single hump in the inter-string interaction energy, while Fe-EAM⁵¹ has a double-hump. All interatomic potentials have ND-core, suggesting the core structure is not solely controlled by the profile of inter-string interaction energy.

Differential displacement plot

Dislocation core structures are visualized using the differential displacement (DD) map between neighboring atoms.⁵² For screw components (Fig. 1, 5, Extended Fig. 9), the arrows are scaled so that the largest components (i.e., $\sim \mathbf{b}/3$) touch the neighboring atoms.

Non-screw components are visualized using the excessive edge component displacement (EECD) (Fig. 3a-d and Extended Data Fig. 8), which is obtained by using the correspond-

ing anisotropic Volterra dislocation field as references. The EECD components of ND-/D-cores possess different symmetry; EECD in D-core has the $\langle 111 \rangle$ threefold screw axis symmetry while that in ND-core has both the $\langle 111 \rangle$ threefold screw axis symmetry and the $\langle 110 \rangle$ diad axis symmetry. The EECD components illustrate the key differences among different materials/models. They are generally very small, and are thus magnified by 6 times.

Atomic configurations (Fig. 3e-h) are visualized using the Open Visualization Tool (OVITO⁵³).

Virtual crystal approximation calculation

Virtual crystal approximation (VCA⁵⁴) calculations are performed using the open source plane wave DFT package, Quantum ESPRESSO (QE⁵⁵). The exchange and correlation functional is described by the generalized gradient approximation (GGA) with the Perdew-Burke-Ernzerhof (PBE³⁵) parameterization. Core electrons are replaced using scalar relativistic ultrasoft pseudo-potentials^{56,57} generated with PSLibrary.⁵⁸ Pseudopotentials for binary alloys are constructed using the atomic concentration weighted average of the pseudopotentials of the constituent pure elements.⁵⁴

For all calculations, the plane-wave function kinetic energy cutoffs and charge density cutoffs are taken as 2041 eV and 24490 eV respectively. The Marzari-Vanderbilt cold smearing⁵⁹ with a width of 0.03 eV is employed. Energy differences between the BCC and FCC structure are calculated using primitive cells with one atom per cell and a Γ -centered $24 \times 24 \times 24$ Monkhorst-Pack k -point mesh.³⁸

Structure optimization is carried out by allowing variations of primitive cell shape, volume, and ion positions. Convergence is assumed when total energy difference between two consecutive steps is less than 1.36×10^{-4} eV and force components on the ion are below 2.57×10^{-3} eV/ \AA . The convergence criterion for electronic self-consistency is 1.36×10^{-7} eV.

Acknowledgements

This work is supported by the Research Grants Council, Hong Kong SAR through the Early Career Scheme Fund under project number 21205019 and Collaborative Research Fund under project number 8730054.

Author Contributions

RW developed interatomic potentials and performed atomistic simulations. LZ calculated core structures using DFT. SP performed VCA calculations. ZW designed and directed the research. ZW and DJS wrote the paper. All authors analysed the data and discussed the results.

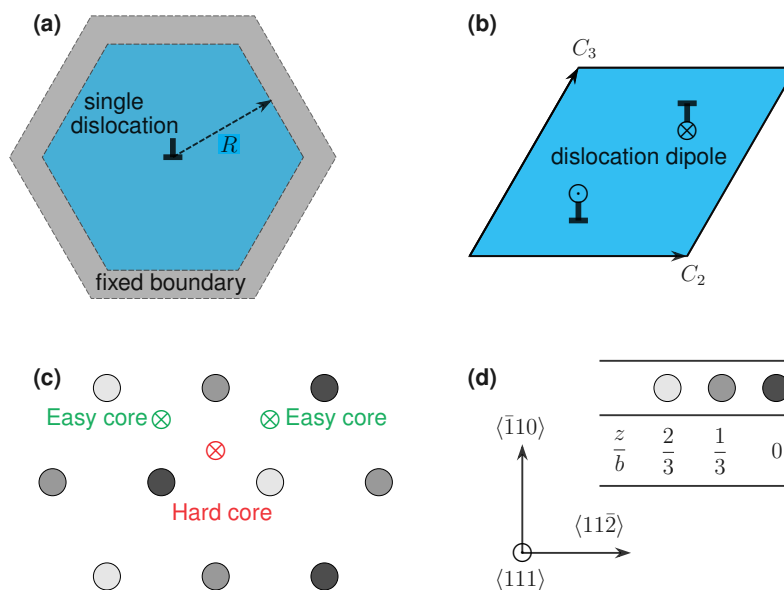
Competing interests

The authors declare no competing interests.

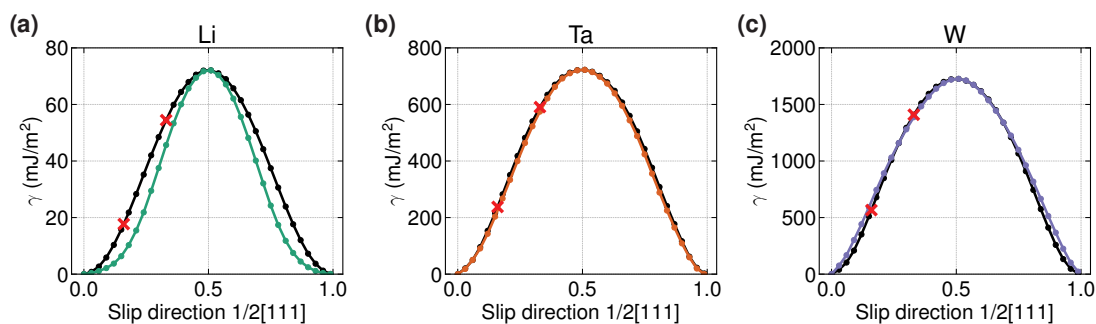
Data Availability

All data are contained in the Methods and Supplementary Information.

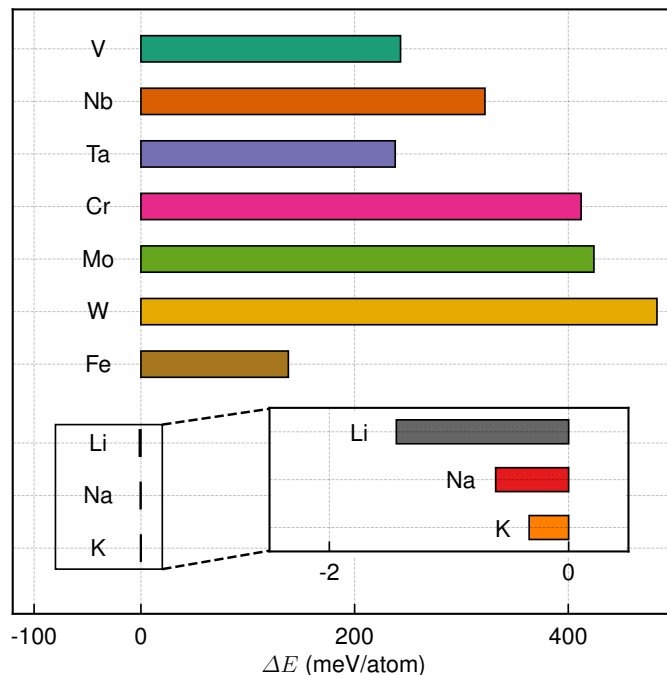
Extended Data



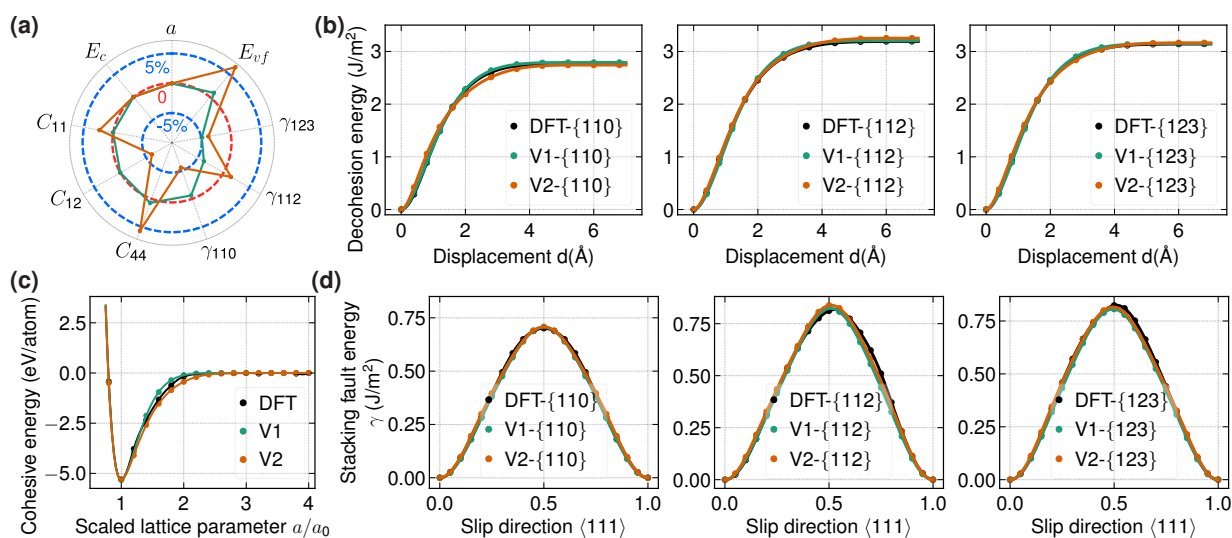
Extended Data Fig. 1 | Supercell for dislocation core simulations. (a) A hexagonal prism with a single dislocation at the center and fixed boundary conditions. (b) Dislocation dipole configuration. (c) Dislocation core center at easy core and hard core positions. (d) Atom color scheme and crystallographic orientations. In (c), atoms are colored based on their positions in the $\langle 111 \rangle$ directions shown in (d).



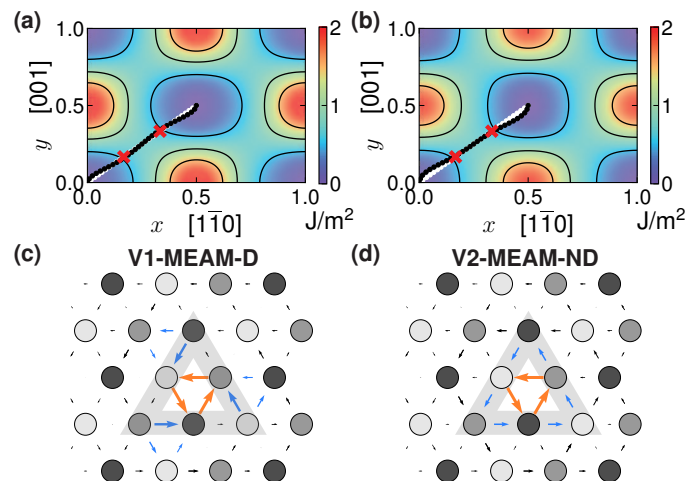
Extended Data Fig. 2 | The generalized stacking fault γ lines along the $\langle 111 \rangle$ direction and minimum energy path (MEP) on the $\{110\}$ plane of BCC Li, Ta and W. The black lines are γ -lines calculated using the classical method and the colored lines are the MEP on the γ -surface shown in Fig. 1d-f. The crosses ("×") denote slips at $b/6$ and $b/3$, respectively. All results are calculated using DFT with parameters in Extended Data Table. 2.



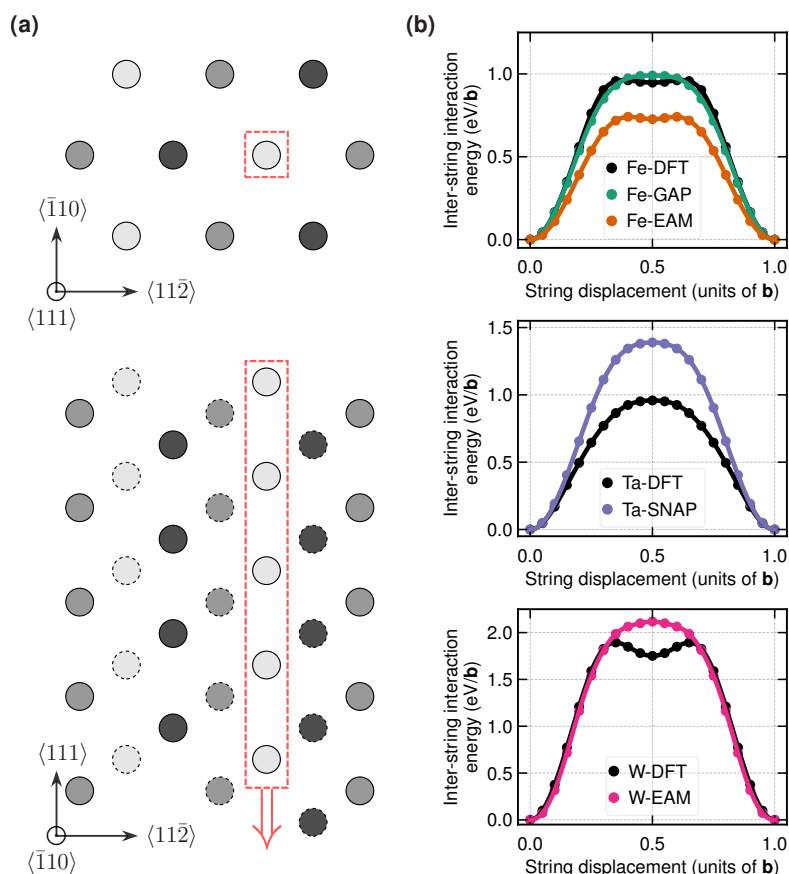
Extended Data Fig. 3 | Energy difference ΔE between the BCC and FCC structure for 7 transition and 3 alkaline metals calculated by DFT. Transition metals have large energy differences $\Delta E > 138$ meV/atom and alkaline metals have vanishingly small energy differences $\Delta E \approx -1$ meV/atom. The calculation parameters are shown in Extended Data Table 2. Exact values of ΔE are shown in Extended Data Table 3.



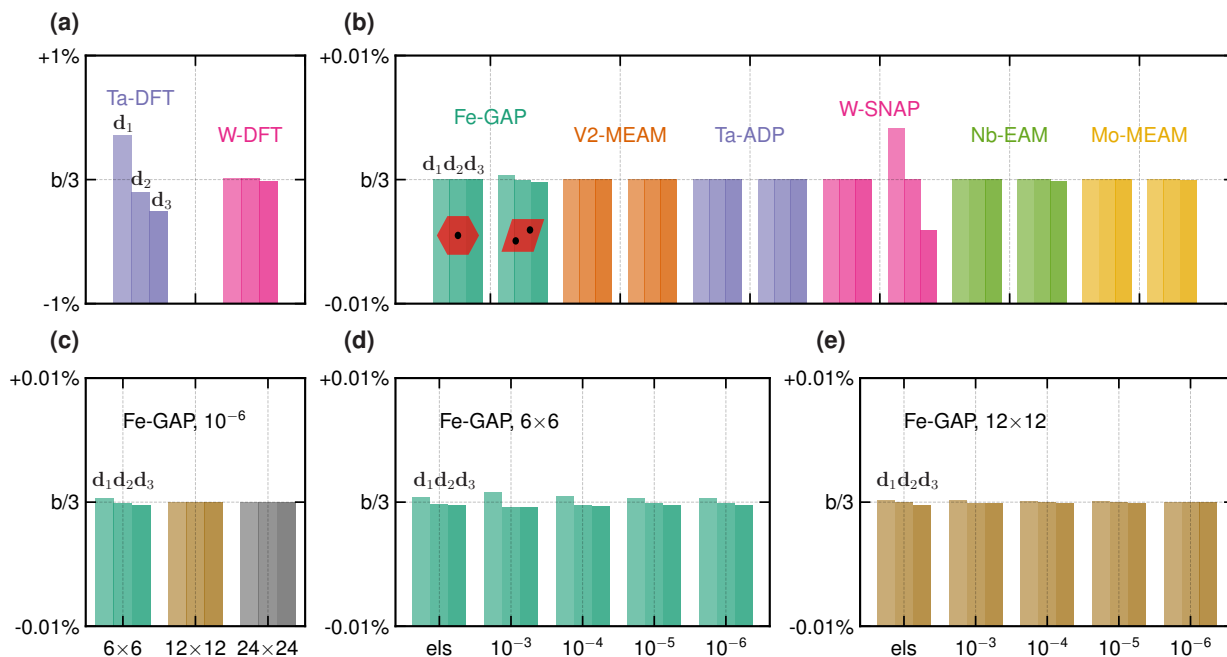
Extended Data Fig. 4 | Properties of two MEAM potentials for V1 and V2. (a) Fitting errors for the lattice parameter, cohesive energy, elastic constants, surface energies and vacancy formation energy for our MEAM potentials V1 and V2. Blue circles are separated by 5% errors. Points closer to or farther from the center than the target means negative or positive errors; (b) Cohesive energy curves; (c) Decohesion energy curves for {110}, {112} and {123} planes; (d) Generalized stacking fault energy curves in the slip direction [111] for {110}, {112} and {123}. All properties are included in the training set.



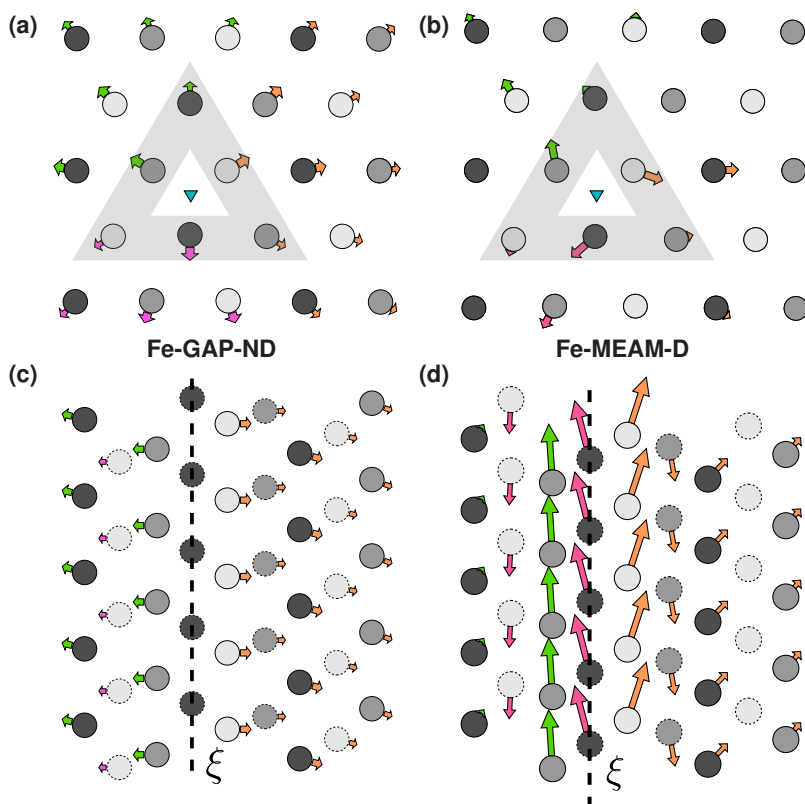
Extended Data Fig. 5 | Generalized stacking fault energy surface and dislocation core structure for two interatomic potentials. Two potentials with nearly identical γ -surfaces (a-b), exhibit a degenerate core (c) and a non-degenerate core (d).



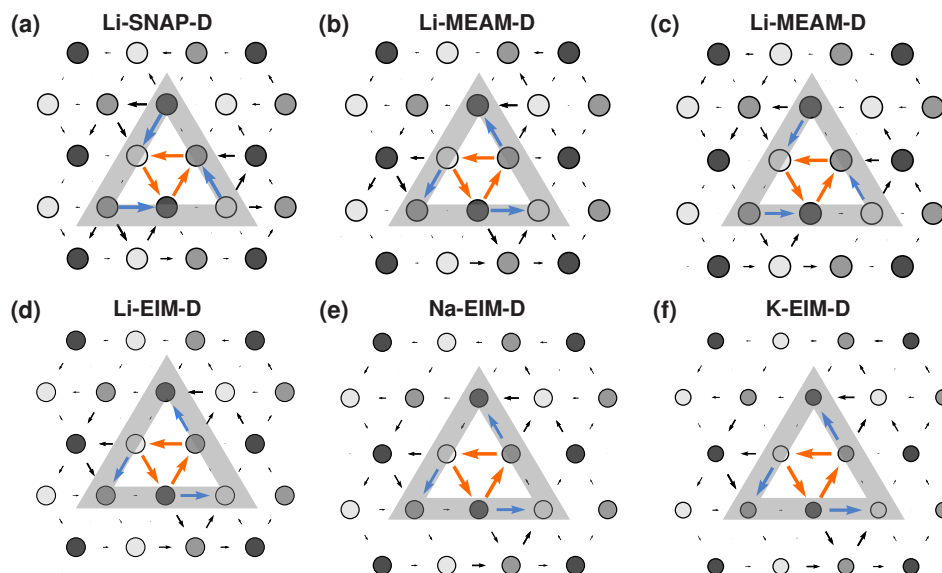
Extended Data Fig. 6 | Supercell model and calculation of inter-string interaction energy. (a) The inter-string model for BCC lattice. A $\langle 111 \rangle$ string atom (in red dashed box) is displaced along $\langle 111 \rangle$ direction while other atoms are fixed. (b) The inter-string interaction energy with displacements along $\langle 111 \rangle$ for Fe, Ta, W calculated by DFT and in comparison with four interatomic potentials (Fe-GAP,²³ Fe-EAM,⁵¹ Ta-SNAP,⁵⁰ W-EAM²⁸). All potentials predict ND-core.



Extended Data Fig. 7 | Size effects on fractional dislocation Burgers vectors. (a) Three fractional Burgers vectors predicted by six interatomic potentials in cluster and dipole models. (b) Supercell size effect of Fe GAP potential in the dipole method. (c,d) Force convergence criterion effect of Fe GAP potential in the dipole method with the supercell size $6 \times 6 \times 1$ and $12 \times 12 \times 1$. The unit is eV/Å. "els" means the initial elastic solution.



Extended Data Fig. 8 | Excessive edge component displacements (EECD) of the screw dislocation calculated by two interatomic potentials. The crystallographic orientation is shown in Fig. 3. The arrows represent the EECD and are magnified by 6 times for comparisons. The two potentials, Fe-GAP²³ and Fe-MEAM,²⁹ give $\Delta E = 159$ meV/atom ($\chi = 1.15$) and $\Delta E = 44$ meV/atom ($\chi = 0.32$), respectively. The Fe-GAP potential exhibits a ND-core with small EECD and Fe-MEAM has a D-core with substantial EECD in $\langle 110 \rangle$ direction on $\{110\}$ planes, consistent with the χ -model prediction.



Extended Data Fig. 9 | Core structures of alkaline metals calculated by the SNAP, EIM and MEAM interatomic potentials and visualized by the differential displacement map. (a) Li-SNAP,⁶⁰ $\Delta E = 2.3$ meV/atom. (b) Li-MEAM,⁶¹ $\Delta E = 1.4$ meV/atom. (c) Li-MEAM,⁶² $\Delta E = 2.1$ meV/atom. (d) Li-EIM, $\Delta E = -23.5$ meV/atom. (e) Na, $\Delta E = -21.4$ meV/atom. (f) K, $\Delta E = -15.5$ meV/atom. All potentials exhibit D-cores. The potentials in (d-f) are developed by Zhou. X.⁶³

Element	Potential formulation and reference	No. of Potentials	
V	EAM, ⁶⁴ MEAM, ^{65,66} BOP, ⁶⁷ GAP ⁶⁸ V1, V2	7	
Nb	EAM, ^{19,69} MEAM, ^{65,70} BOP, ⁶⁷ ADP, ⁷¹ SNAP, ⁵⁰ GAP ⁶⁸	8	
Ta	EAM, ⁷²⁻⁷⁵ MEAM, ⁶⁵ BOP, ⁶⁷ ADP, ⁷⁶ SNAP, ^{50,77} GAP ⁶⁸	10	
Transition metals	Cr	EAM, ⁷⁸ MEAM, ⁷⁹ BOP, ⁶⁷ ADP ⁸⁰	4
Mo	EAM, ^{74,81} MEAM, ^{65,82,83} BOP, ⁶⁷ ADP, ⁸⁴ SNAP, ^{50,60,85} GAP ⁶⁸	11	
W	EAM, ^{28,74,75,86-88} MEAM, ^{65,89,90} BOP, ⁶⁷ SNAP, ⁵⁰ GAP ⁶⁸	12	
Fe	EAM, ^{3,51,74,86,91-98} MEAM, ^{29,65,99,100} BOP, ¹⁰¹ ReaxFF, ¹⁰² GAP, ²³ ANN ¹⁰³	20	
Alkaline metals	Li	EIM, ⁶³ MEAM, ^{61,62} SNAP ⁶⁰	4
Na	EIM ⁶³	1	
K	EIM ⁶³	1	

Extended Data Table 1 | Interatomic potentials for seven transition and three alkaline metals used in this work.

Calculations	Element	Valence states	Cutoff energy (eV)	k -mesh (unitcell)	Sigma
Energy difference ΔE	V	$3s^2 3p^6 3d^4 4s^1$	550	$21 \times 21 \times 21$	0.2
	Nb	$4s^2 4p^6 4d^4 5s^1$	550	$19 \times 19 \times 19$	0.1
	Ta	$5p^6 5d^4 6s^1$	550	$19 \times 19 \times 19$	0.1
	Cr	$3s^2 3p^6 3d^5 4s^1$	600	$22 \times 22 \times 22$	0.1
	Mo	$4s^2 4p^6 4d^5 5s^1$	600	$20 \times 20 \times 20$	0.1
	W	$5s^2 5p^6 5d^5 6s^1$	550	$20 \times 20 \times 20$	0.05
	Fe	$3s^2 3p^6 3d^7 4s^1$	700	$23 \times 23 \times 23$	0.05
	Li	$2s^1$	400	$19 \times 19 \times 19$	0.2
	Na	$2p^6 3s^1$	550	$31 \times 31 \times 31$	0.2
	K	$3s^2 3p^6 4s^1$	550	$24 \times 24 \times 24$	0.2
Dislocation core, γ -surface	Ta	$5d^4 6s^1$	550	$24 \times 24 \times 24$	0.2
	W	$5d^5 6s^1$	550	$31 \times 31 \times 31$	0.2

Extended Data Table 2 | Valence states, plane wave energy cutoffs, k-mesh densities and smearing parameters used in the DFT calculations.

Element	Structure energy difference ΔE (meV/atom)
Transition metals	
V	243
Group V	Nb 322
	Ta 238
Group VI	Cr 412
	Mo 424
	W 483
Group VIII	Fe 138
Alkaline metals	
Li	-1.44
Na	-0.61
K	-0.33

Extended Data Table 3 | Energy difference of transition metals in BCC and FCC structures. The FCC structure is highly unfavourable ($\Delta E > 138$ meV/atom) in all transition metals, while alkaline metals have negligibly small energy difference between the BCC and FCC structures.

Element	E_c	r_e	α	β^0	β^1	β^2	β^3	t^1	t^2	t^3
Li	1.6700	3.0233	3.1636	1.7854	1.2538	4.5937	2.9397	4.1275	3.3688	0.2672
V1	5.3100	2.6154	4.7719	4.9475	2.7601	4.4149	3.2709	4.7765	-3.9531	2.5272
V2	5.3100	2.6154	4.7283	5.6477	5.5320	2.3578	2.3319	5.9285	-7.2050	4.9702
Element	A	C_{\min}	C_{\max}	d_{repuls}	d_{attrac}	r_e	Δr			
Li	1.0109	0.0006	2.7284	0.0795	0.0047	6.6521	4.0468			
V1	0.5562	0.1838	3.0049	0.0134	-0.0259	7.5334	5.2633			
V2	0.4915	0.2286	3.0239	0.0208	0.0554	7.8342	5.5395			

Extended Data Table 4 | Parameters of new MEAM interatomic potentials for Li and V (V1, V2). The units of the cohesive energy E_c and equilibrium distance r_e are eV and Å, respectively.

Supplementary Information

Size effects in core structure calculations

887

888

889 In the screw dislocation of BCC metals, the three fractional dislocation Burgers vectors \mathbf{d}_k enclosing the core are thought to be
 890 identical.^{25,104,105} Atomistic calculations of core structures also report equal splitting in the core center. This assertion, however,
 891 has not been carefully examined, at least in DFT calculations. In the dipole-configuration, we find the three fractional Burgers
 892 vectors, in the D or ND-core, are not quantitatively identical. This appears to violate the non-degeneracy term given to the ND-
 893 core. We also find that the anisotropic elastic solution gives small differences in \mathbf{d}_k , with two of them nearly identical and the
 894 third one distinctly different. The dipole-configuration, would thus never result in a true ND-core, as visible in some of the earlier
 895 reported studies (e.g., cf. Fig. 1a-c in Ref.⁷).

896 The differences in \mathbf{d}_k are a result of supercell size and/or convergence tolerance in the calculations, and not intrinsic to the
 897 core property. Extended Data Fig. 7a shows the three fractional Burgers vectors \mathbf{d}_k calculated using the cluster method and the
 898 dipole method, using 6 interatomic potentials (GAP for Fe,²³ V2-MEAM for V, ADP for Ta,⁷⁶ SNAP for W,⁵⁰ EAM for Nb⁶⁹
 899 and MEAM for Mo⁸²). In each case, the cluster-method always gives identical fractional Burgers vector, i.e., $\mathbf{d}_1 = \mathbf{d}_2 = \mathbf{d}_3$.
 900 The screw component of each \mathbf{d}_k is precisely $\mathbf{b}/3$. The edge components of the three \mathbf{d}_k have the same magnitude but different
 901 orientation. They sum to zero and satisfy both the $\langle 110 \rangle$ -diad and $\langle 111 \rangle$ three-fold symmetry. Therefore, the compact core obtained
 902 from the cluster-method is precisely non-degenerate. However, the cores obtained in the dipole-method have different \mathbf{d}_k , similar
 903 to that of the elastic solution. Similar observation is also seen in the core calculation of Ta and W using DFT (Extended Data
 904 Fig. 7a).

905 The differences in \mathbf{d}_k in the dipole method reduces with increasing supercell size (Fig. 7c) and convergence tolerance (Fig. 7d-e).
 906 However, these supercell sizes and convergence tolerances are difficult to achieve in routine DFT calculations.

907

Three special cases

908 Three potentials (Nb-SNAP,⁵⁰ Cr-EAM⁷⁸ and Mo-ADP⁸⁴) examined in the current work do not follow the χ model prediction.
 909 Nb-SNAP has $\Delta E = 111$ meV/atom and BCC elastic constants $C_{11} = 253$ GPa, $C_{12} = 136$ GPa and $C_{44} = 14$ GPa, while
 910 DFT shows $\Delta E = 322$ meV/atom and BCC elastic constants are $C_{11} = 253$ GPa, $C_{12} = 133$ GPa and $C_{44} = 31$ GPa from
 911 the experiments. Cr-EAM has $\Delta E = 10$ meV/atom and a meta stable FCC structure with $C_{11} = 585$ GPa, $C_{12} = 302$ GPa,
 912 $C_{44} = 212$ GPa, while DFT predicts $\Delta E = 412$ meV/atom and the FCC structure is unstable. Mo-ADP has $\Delta E = 363$
 913 meV/atom and BCC elastic constants $C_{11} = 547$ GPa, $C_{12} = 168$ GPa, $C_{44} = 160$ GPa, while DFT shows $\Delta E = 424$ meV/atom
 914 and BCC elastic constants from experiments are $C_{11} = 472$ GPa, $C_{12} = 158$ GPa, $C_{44} = 106$ GPa. The three potentials thus have
 915 basic properties largely different from DFT calculations or experimental measurements. These interatomic potentials appear to
 916 be less physical and can not reasonably represent the elementary metals, respectively, which may be responsible for their unusual
 917 behaviours.